Multiple topological states in iron-based superconductors

Peng Zhang [1]*, Zhijun Wang [2], Xianxin Wu [3], Koichiro Yaji [1], Yukiaki Ishida [1], Yoshimitsu Kohama [1], Guangyang Dai [4], Yue Sun [1,5], Cedric Bareille [1], Kenta Kuroda [1], Takeshi Kondo [1], Kozo Okazaki [1], Koichi Kindo [1], Xiancheng Wang [4], Changqing Jin [4], Jiangping Hu [4,6], Ronny Thomale [3], Kazuki Sumida [7], Shilong Wu [8], Koji Miyamoto [8], Taichi Okuda [8], Hong Ding [4,6], G. D. Gu [9], Tsuyoshi Tamegai [5], Takuto Kawakami [10], Masatoshi Sato [10] and Shik Shin [1]*

[1]Institute for Solid State Physics, University of Tokyo, Kashiwa, Japan. [2]Department of Physics, Princeton University, Princeton, NJ, USA. [3]Institut für Theoretische Physik und Astrophysik, Julius-Maximilians-Universität Würzburg, Würzburg, Germany. [4]Beijing National Laboratory for Condensed Matter Physics and Institute of Physics, Chinese Academy of Sciences, Beijing, China. [5]Department of Applied Physics, University of Tokyo, Tokyo, Japan. [6]CAS Center for Excellence in Topological Quantum Computation, University of Chinese Academy of Sciences, Beijing, China. [7]Graduate School of Science, Hiroshima University, Higashi-Hiroshima, Japan. [8]Hiroshima Synchrotron Radiation Center, Hiroshima University, Higashi-Hiroshima, Japan. [9]Condensed Matter Physics and Materials Science Department, Brookhaven National Laboratory, Upton, NY, USA. [10]Yukawa Institute for Theoretical Physics, Kyoto University, Kyoto, Japan. *e-mail: zhangpeng@issp.u-tokyo.ac.jp; shin@issp.u-tokyo.ac.jp

Supplementary Information for "Multiple topological states in iron-based superconductors"

Peng Zhang,[1] Zhijun Wang,[2] Xianxin Wu,[3] Koichiro Yaji,[1] Yukiaki Ishida,[1] Yoshimitsu Kohama,[1] Guangyang Dai,[4] Yue Sun,[1,5] Cedric Bareille,[1] Kenta Kuroda,[1] Takeshi Kondo,[1] Kozo Okazaki,[1] Koichi Kindo,[1] Xiancheng Wang,[4] Changqing Jin,[4] Jiangping Hu,[4,6] Ronny Thomale,[3] Kazuki Sumida,[7] Shilong Wu,[8] Koji Miyamoto,[8] Taichi Okuda,[8] Hong Ding,[4,6] G.D. Gu,[9] Tsuyoshi Tamegai,[5] Takuto Kawakami,[10] Masatoshi Sato,[10] and Shik Shin[1]

[1]*Institute for Solid State Physics, University of Tokyo, Kashiwa, Chiba 277-8581, Japan*
[2]*Department of Physics, Princeton University, Princeton, New Jersey 08544, USA*
[3]*Institut für Theoretische Physik und Astrophysik,*
Julius-Maximilians-Universität Würzburg, Würzburg, 97074, Germany
[4]*Beijing National Laboratory for Condensed Matter Physics and Institute of Physics,*
Chinese Academy of Sciences, Beijing 100190, China
[5]*Department of Applied Physics, University of Tokyo, Bunkyo-ku, Tokyo 113-8656, Japan*
[6]*CAS Center for Excellence in Topological Quantum Computation,*
University of Chinese Academy of Sciences, Beijing 100190, China
[7]*Graduate School of Science, Hiroshima University, Higashi-Hiroshima 739-8526, Japan*
[8]*Hiroshima Synchrotron Radiation Center, Hiroshima University, Higashi-Hiroshima 739-0046, Japan*
[9]*Condensed Matter Physics and Materials Science Department,*
Brookhaven National Laboratory, Upton, NY 11973, USA
[10]*Yukawa Institute for Theoretical Physics, Kyoto University, Kyoto 606-8502, Japan*

I. EXPERIMENTAL SETUPS

The high-resolution ARPES and the spin-resolved ARPES used for this project have different experimental geometries, as shown in Fig.S1. Since the photons with polarization along z direction is suitable for detecting p_z and d_{z^2} orbitals, p polarized photons are used for the measurements of topological surface states. The experimental geometry of the spin-resolved ARPES (Setup II) is asymmetric respect to M_y plane, which induces an asymmetric intensity pattern in the ARPES spectrum, as shown in Fig.3(a,e,i).
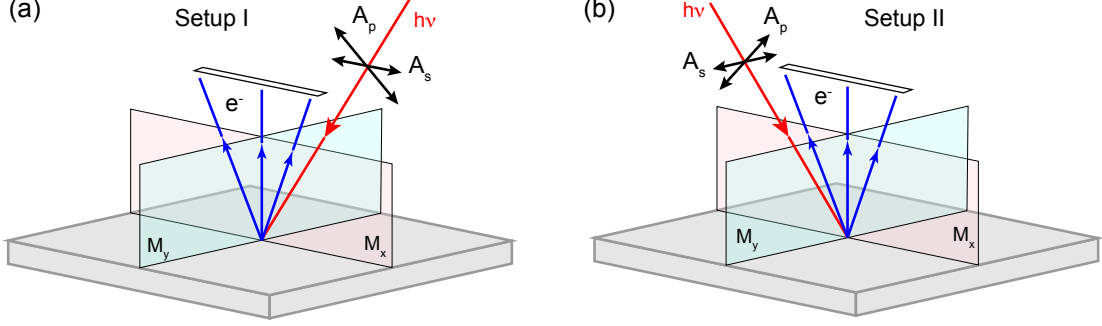

FIG. S1. **Experimental setups.** (a - b) Experimental geometries of the high-resolution ARPES (Setup I) and spin-resolved ARPES (Setup II), respectively.

II. SPIN HELICITY OF THE SURFACE STATES IN LI(FE,CO)AS

Because of the spin-momentum locking, the topological states should show a spin-helical texture, as displayed in Fig. S2(a). In the main text, EDCs at Cut 1 and Cut 2 along k_y direction were measured to avoid the intensity asymmetry mentioned above, of which the spin polarizations are consistent with the calculated spin-helical texture. To further confirm the spin helicity of the surface states, we also measured another two EDCs at CutS1 and CutS2 along k_x direction, as shown in Fig. S2(b - c). Despite the intensity asymmetry, the spin polarizations in Fig. S2(d) are consistent with the spin-helical texture in Fig. S2(a).
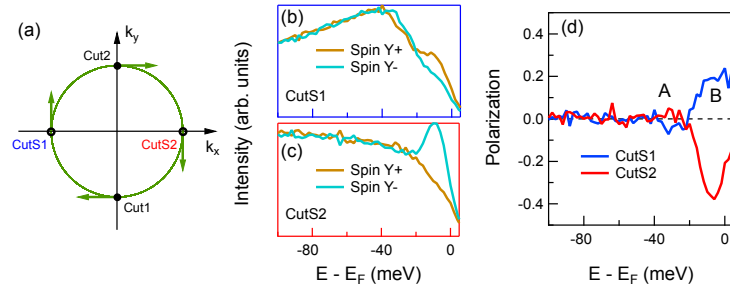

FIG. S2. **Spin polarization of the TI surface Dirac cone along k_x direction in Li(Fe$_{1-x}$Co$_x$)As ($x = 3\%$).** (a) Sketch of the spin helicity of the TI surface cone. Data for Cut1 and Cut2 are shown in Fig.3. (b - c) Spin resolved EDCs at CutS1 and CutS2 measured with 7-eV laser. (d) Spin polarization curves of EDCs at CutS1 and CutS2.

III. SUPERCONDUCTING GAP OF THE SURFACE STATES IN LIFEAS

According to the theory [1], if the spin-helical surface states open an s-wave superconducting gap, the surface states will be topologically superconducting and will host Majorana bound states in the vortices. However, the TI surface

band in $LiFe_{1-x}Co_xAs$ ($x = 3\%$) does not cross Fermi level. Thus we studied LiFeAs without Co doping for surface topological superconductivity. The TI surface band crosses E_F in LiFeAs samples, as shown in Fig. S3(a). The gap size gradually closes as temperature increases, confirming the superconducting origin of the gap. In Fig. S3(c - d), no momentum-dependence of the superconducting gap is observed, indicating an s-wave gap, which is consistent with the isotropic bulk gaps. Generally, these evidences would support the existence of topological superconductivity on the surface. However, as shown in Fig. 2(d), the TI surface band overlaps with some bulk states, which may induce a topological phase transition on the surface band to trivial superconductivity [2, 3]. The influence of the bulk states and the possible topological phase transition can be studied by STM with different doping levels [2, 3]. We also notice that the TI surface band in LiFeAs may not cross E_F with more electron doping [Fig. 2(e)]. Instead, hole doping in LiFeAs may be a more promising way to have surface topological superconductivity and Majorana bound states.
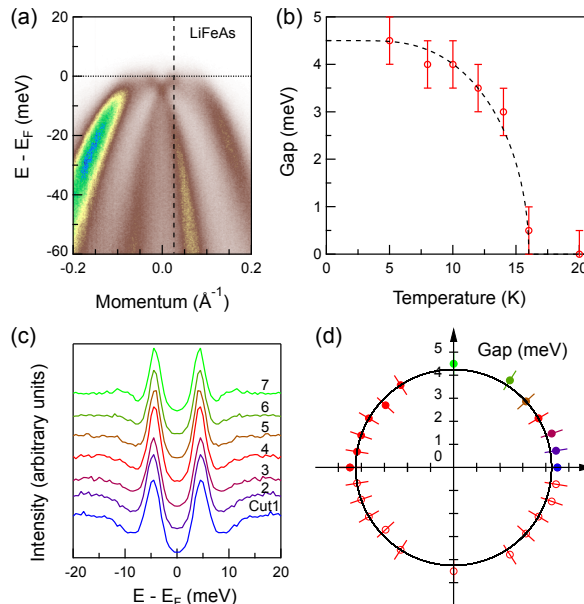

FIG. S3. **Superconducting gap of the TI surface band in LiFeAs.** (a) Intensity plot of band structure measured at 20 K, with a p polarized 7-eV laser. (b) Superconducting gap size of the surface band as a function of temperature. (c) The symmetrized EDCs at different k_F of the surface band, measured at 5 K. The positions of the EDCs on the Fermi surface are indicated by the dots with the corresponding colors in (d). (d) Polar representation of the superconducting gap size of the surface band.

IV. BAND STRUCTURE OF FE(TE,SE)

The band structure at the Γ point measured with Setup II is displayed in Fig. S4. In line with previous reports [4–6], three t_{2g} bonding bands from Fe $3d$ orbitals are observed near E_F. From the curvature intensity plot [7] of the energy-distribution curves (EDC) in Fig. S4(b), we demonstrate that only the band with d_{yz} orbital character crosses E_F and forms a hole pocket, while the band with d_{xy} orbital character is very likely below E_F [6]. The splitting of the d_{xz} and d_{yz} bands at Γ is induced by spin-orbit coupling (SOC). However, the SOC hybridization between the d_{xy} and d_{yz} bands is difficult to identify in Fig. S4 due to the low resolution. With high energy and momentum resolutions from laser-ARPES, this hybridization is clearly unveiled [Fig. 4(a)].

V. THE EFFECTIVE K·P MODEL HAMILTONIAN FOR FE(TE,SE)

A. The $k \cdot p$ model without SOC

Following our previous theoretical paper [8], the (x,y) axes are rotated by $45°$ as compared to the crystallographic axes. In other words, the Fe-Fe direction is the x direction in our convention. We first construct a $k \cdot p$ model at
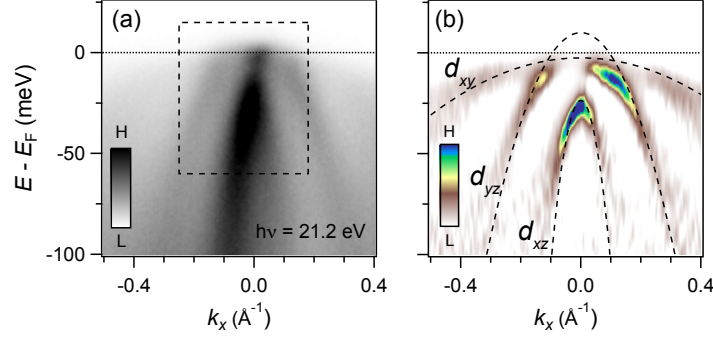
FIG. S4. **Band structure of FeTe$_{0.55}$Se$_{0.45}$ at Γ.** (a) Intensity plot of band structure measured with h$\nu = 21.2$eV from a helium discharge lamp. (b) EDC curvature plot of (a). The dashed lines are guide lines to the d_{xy}, d_{yz} and d_{xz} bands.

the Γ point without SOC. In ref. [8], the first-principles calculations indicate the bands near the Fermi level (E_F) at Γ belong to irreducible representations (irreps) of Γ_2^-, Γ_5^+, and Γ_4^+. According to the character table of D_{4h}, the point-group symmetry at Γ, the representative bases are $|z\rangle$, $|yz/xz\rangle$ and $|xy\rangle$, respectively. Thus, the low-energy effective Hamiltonian of Fe(Te,Se) can be captured by a 4-band $k \cdot p$ invariant model at Γ.

The representatives of D_{4h} have inversion symmetry (P), 4-fold rotational symmetry about the z-axis (C_4), 2-fold rotational symmetry about the x-axis (C_{2x}), and 2-fold rotational symmetry about the xy-direction ($C_{2,11}$). Under the basis of $|z\rangle$, $|yz\rangle$, $|xz\rangle$ and $|xy\rangle$, they are presented explicitly as follows:

$$
P = \begin{pmatrix} -1 & 0 & 0 & 0 \\ 0 & 1 & 0 & 0 \\ 0 & 0 & 1 & 0 \\ 0 & 0 & 0 & 1 \end{pmatrix}, \quad
C_4 = \begin{pmatrix} 1 & 0 & 0 & 0 \\ 0 & 0 & 1 & 0 \\ 0 & -1 & 0 & 0 \\ 0 & 0 & 0 & -1 \end{pmatrix}, \quad
C_{2x} = \begin{pmatrix} -1 & 0 & 0 & 0 \\ 0 & 1 & 0 & 0 \\ 0 & 0 & -1 & 0 \\ 0 & 0 & 0 & -1 \end{pmatrix}, \quad
C_{2,11} = \begin{pmatrix} -1 & 0 & 0 & 0 \\ 0 & 0 & -1 & 0 \\ 0 & -1 & 0 & 0 \\ 0 & 0 & 0 & 1 \end{pmatrix}.
$$

Those operators acting on momentum space ((k_x, k_y, k_z)) are given by the following matrices, respectively.

$$
\hat{p} = \begin{pmatrix} -1 & 0 & 0 \\ 0 & -1 & 0 \\ 0 & 0 & -1 \end{pmatrix}, \quad
\hat{c}_4 = \begin{pmatrix} 0 & -1 & 0 \\ 1 & 0 & 0 \\ 0 & 0 & 1 \end{pmatrix}, \quad
\hat{c}_{2x} = \begin{pmatrix} 1 & 0 & 0 \\ 0 & -1 & 0 \\ 0 & 0 & -1 \end{pmatrix}, \quad
\hat{c}_{2,11} = \begin{pmatrix} 0 & 1 & 0 \\ 1 & 0 & 0 \\ 0 & 0 & -1 \end{pmatrix},
$$

Also, time reversal symmetry is represented as $T = \mathbb{I}_{4\times4}\mathcal{K}$ with $\mathcal{K}$ the complex conjugation in the real-functional basis and $\hat{t} = Diag[-1, -1, -1]$ in momentum space. Using the constraints $RH(\hat{r}^{-1}\mathbf{k})R^{-1} = H(\mathbf{k})$ (R stands for all the symmetry operations mentioned above), the time-reversal-invariant $k \cdot p$ Hamiltonian at Γ is derived as (up to the second order):

$$
H_0(\mathbf{k}) = \begin{pmatrix}
M_1(\mathbf{k}) & i\chi k_y & i\chi k_x & 0 \\
-i\chi k_y & M_2(\mathbf{k}) + \beta(k_x^2 - k_y^2) & \alpha k_x k_y & \gamma k_x k_z \\
-i\chi k_x & \alpha k_x k_y & M_2(\mathbf{k}) - \beta(k_x^2 - k_y^2) & \gamma k_y k_z \\
0 & \gamma k_x k_z & \gamma k_y k_z & M_3(\mathbf{k})
\end{pmatrix},
$$

where $M_i(k) = M_0^i + M_1^i(k_x^2 + k_y^2) + M_2^i k_z^2$.

B. The $k \cdot p$ model with SOC

To include the spin degree of freedom, we redefine the real-functional basis with definite C_4 eigenvalues $(+1, +i, -i, +1)$ for convenience. Then, the model is rewritten and the unitary transforming matrix is given as follows,

$$H_0'(\mathbf{k}) = U^{-1} H_0(\mathbf{k}) U$$

$$= \begin{pmatrix} M_1(\mathbf{k}) & -\chi k_-/\sqrt{2} & \chi k_+/\sqrt{2} & 0 \\ -\chi k_+/\sqrt{2} & M_2(\mathbf{k}) & \beta(k_x^2 - k_y^2) - i\alpha k_x k_y & \gamma k_z k_-/\sqrt{2} \\ \chi k_-/\sqrt{2} & \beta(k_x^2 - k_y^2) + i\alpha k_x k_y & M_2(\mathbf{k}) & \gamma k_z k_+/\sqrt{2} \\ 0 & \gamma k_z k_+/\sqrt{2} & \gamma k_z k_-/\sqrt{2} & M_3(\mathbf{k}) \end{pmatrix},$$

where $k_\pm = k_x \pm i k_y$;

$$U = \begin{pmatrix} 1 & 0 & 0 & 0 \\ 0 & 1/\sqrt{2} & 1/\sqrt{2} & 0 \\ 0 & i/\sqrt{2} & -i/\sqrt{2} & 0 \\ 0 & 0 & 0 & 1 \end{pmatrix}.$$

The full Hamiltonian with SOC takes the form $H(\mathbf{k}) = \mathbb{I}_2 \otimes H_0'(\mathbf{k}) + H_{soc}$ under the spinful bases $(|\uparrow\rangle, |\downarrow\rangle) \otimes (|1\rangle, |2\rangle, |3\rangle, |4\rangle)$. Here, the H_{soc} is given [3] by

$$H_{soc}(\mathbf{k}) = \begin{pmatrix} 0 & 0 & 0 & 0 & 0 & 0 & \sqrt{2}k_z\lambda_3 & 0 \\ 0 & -\lambda_1 & 0 & 0 & \sqrt{2}k_z\lambda_3 & 0 & 0 & 0 \\ 0 & 0 & \lambda_1 & 0 & 0 & 0 & 0 & -\sqrt{2}\lambda_2 \\ 0 & 0 & 0 & 0 & 0 & \sqrt{2}\lambda_2 & 0 & 0 \\ 0 & \sqrt{2}k_z\lambda_3 & 0 & 0 & 0 & 0 & 0 & 0 \\ 0 & 0 & 0 & \sqrt{2}\lambda_2 & 0 & \lambda_1 & 0 & 0 \\ \sqrt{2}k_z\lambda_3 & 0 & 0 & 0 & 0 & 0 & -\lambda_1 & 0 \\ 0 & 0 & -\sqrt{2}\lambda_2 & 0 & 0 & 0 & 0 & 0 \end{pmatrix}$$

which does not break inversion symmetry.

The bulk band structure along $\Gamma - Z$ in Fig. S5(a) is calculated with the Hamiltonian obtained by substituting $sin(k_z \cdot c)/c$ and $2[1 - cos(k_z \cdot c)]/c^2$ for k_z and k_z^2 respectively in $H(\mathbf{k})$, with the lattice constant $c = 5.9552$ Å. After including SOC, the doubly-degenerate Γ_5^+ bands split into two d_{xz}/d_{yz} bands, and the Γ_4^+ and Γ_2^- bands become d_{xy} and p_z bands, respectively.

The (001) surface spectra in Fig. 4(b) are calculated by the surface Green's function method. In order to simulate the surface effect, we add a surface Rashba SOC term ($H_R(\mathbf{k})$) to the full Hamiltonian $H(\mathbf{k})$, which reads

$$H_R(\mathbf{k}) = \begin{pmatrix} 0 & 0 & 0 & 0 & 0 & 0 & 0 & 0 \\ 0 & 0 & 0 & 0 & 0 & -i\lambda_R k_- & 0 & 0 \\ 0 & 0 & 0 & 0 & 0 & 0 & -i\lambda_R k_- & 0 \\ 0 & 0 & 0 & 0 & 0 & 0 & 0 & 0 \\ 0 & 0 & 0 & 0 & 0 & 0 & 0 & 0 \\ 0 & i\lambda_R k_+ & 0 & 0 & 0 & 0 & 0 & 0 \\ 0 & 0 & i\lambda_R k_+ & 0 & 0 & 0 & 0 & 0 \\ 0 & 0 & 0 & 0 & 0 & 0 & 0 & 0 \end{pmatrix}$$

The parameters used in the calculations are given as follows:

0.04	2.40	-0.8		::	m_0^1	m_1^1	m_2^1
0.000	-3.80	0.14		::	m_0^2	m_1^2	m_2^2
-0.002	-0.2	0.002		::	m_0^3	m_1^3	m_2^3
-4.40	2.2	0.004	0.412	::	α	β	γ	χ
0.0105	0.003	0.019	0.005	::	λ_1	λ_2	λ_3	λ_R

C. The SOC and orbital characters

Without SOC, each of the d_{xy}, d_{yz} and d_{xz} bands near E_F consists of a single orbital along ΓM. However, the SOC hybridizes the bands and mixes the orbital characters. It is no longer precise to distinguish bands with orbitals.

The more accurate way is to specify the weight of each orbital in one band. The band structure of d_{xy}, d_{yz} and d_{xz} bands along ΓM in the $k \cdot p$ model is displayed in Fig. S5(a), and the weight of different orbitals in different bands is displayed in Fig. S5(b - d).
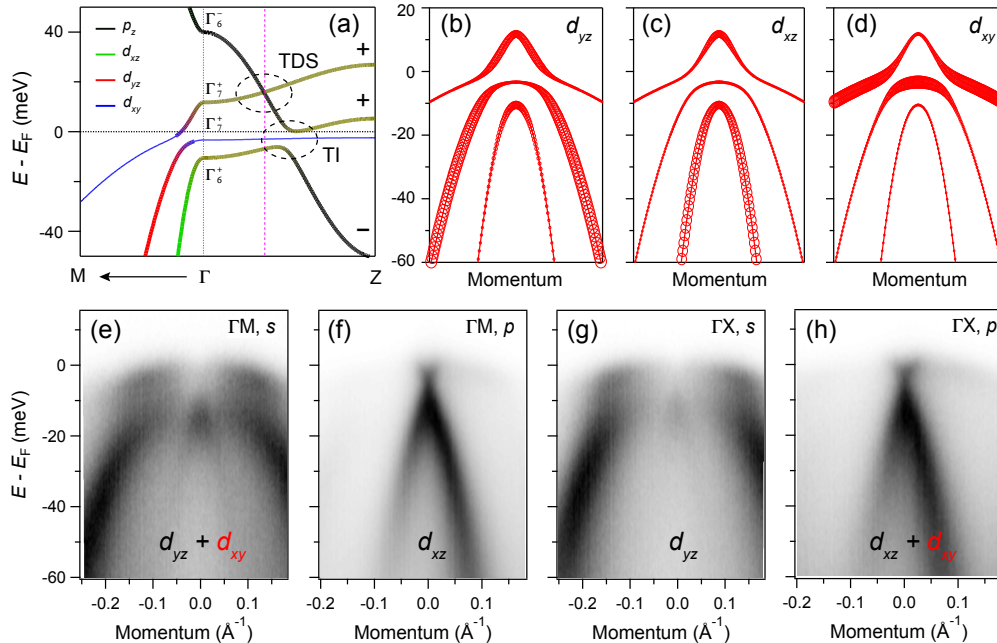

FIG. S5. **Orbital characters of bands in Fe(Te,Se).** (a) Band structure along ΓM and ΓZ. (b - d) Orbital characters of the α, β and γ bands. (e - h) Intensity plots of the band structure with different photon-polarizations and sample orientations from ARPES experiments. Note that the Dirac-cone in (f) and (h) comes from surface states.

The photoelectron intensities of the bands vary with sample orientations and photon polarizations because of the matrix element effect, which is widely used in ARPES to check the orbital characters. According to the matrix element effect, with the experimental geometry Setup II displayed in Fig. S1(b), the visible orbitals should be d_{yz} and d_{xy} for ΓM orientation and s polarized photons (ΓM + s), d_{xz} for ΓM + p, d_{yz} for ΓX + s, d_{xz} and d_{xy} for ΓX + p. The experimental results with ΓM/ΓX orientations and s/p polarizations are shown in Fig. S5(e - h). The d_{yz} orbital is visible with ΓM + s and ΓX + s configurations, while d_{xz} orbital is visible with ΓM + p and ΓX + p configurations. d_{xy} orbital is not observed with neither ΓM + s nor ΓX + p configuration, since it has a very weak intensity for a small momentum range near Γ. We note that Fig. S5(e)(g) match well with Fig. S5(b), and Fig. S5(f)(h) match well with Fig. S5(c).

VI.   HELICITY OF THE SURFACE STATES FROM TDS

The $k \cdot p$ model in Part V involves both TI and TDS states. By isolating the two inverted bands, we can study the spectrum of TI or TDS states separately, as shown in Fig.1(a-c). By adjusting the model parameters, we found that the helicity of the (001) surface states in TDS is not intrinsic. The relative positions of the two inverted bands may change the helicity of the surface states, as shown in Fig. S6. The spin polarization of the TDS surface states may also be affected by the surface Rashba interaction [9].

VII.   SPIN-POLARIZED BACKGROUND

A constant spin polarization at the background part of EDCs was observed for the spin-polarization measurements. In Fig. S7, we displayed one set of data from Fe(Te,Se) to illustrate this osbervation. The constant spin polarization exists in the background part (< -30 meV) of the EDCs, which may come from the photoemission process, or the spin-matrix element effect. For a better visualization, we normalized the spin-up or spin-down EDC by a constant
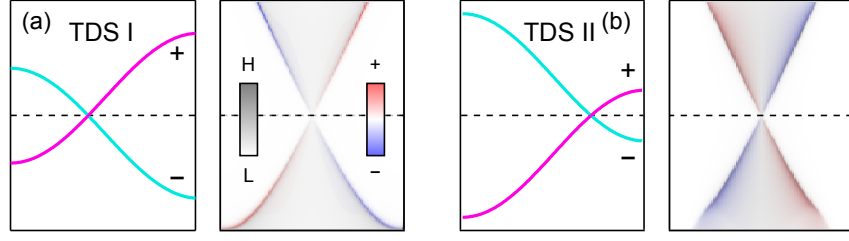
FIG. S6. **Helicity of the TDS surface states.** (a - b) Band structures along k_z and the corresponding (001) surface spectrums. The position difference of the two inverted bands gives different helicities of the surface states. The grey color scales the spin-integrated intensity, while the blue/red colors scale the spin-polarized intensity.

and removed the spin-polarized background for the spin-resolved ARPES results in this report, as shown in Fig. S7(d - e), which does not affect the conclusion of this paper.
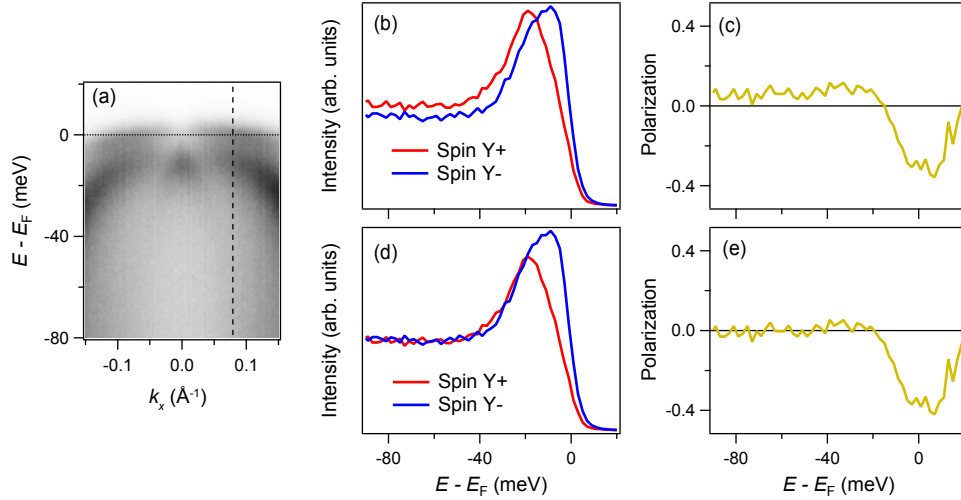

FIG. S7. **Spin-polarized background**. (a) Spin-integrated intensity plot. (b - c) Spin-polarized EDCs and spin polarization curve at the cut indicated in (a). (d - e) Spin-polarized EDCs and spin polarization curve after normalization with a constant.

VIII. PHOTON-POLARIZATION DEPENDENCE OF THE SPIN POLARIZATION

The photoemission process may induce extrinsic spin polarization. The extrinsic spin polarization generally depends on the photon polarizations and the photon energies, while intrinsic spin polarization of the electronic initial states should show the same result for different experimental setups. Thus we measured the spin polarization with different photon polarizations and energies to confirm the intrinsic origin of the spin polarization in Fe(Te,Se). The spin-resolved EDCs at Cut 1 in Fig.5(a) measured with different photon polarizations are shown in Fig. S8(a - d). The experiments with s polarized, circular right (CR) polarized and circular left (CL) polarized photons give the same result. There is no cross section for p polarized photons, as shown in Fig. S5(f)(h).Thus the corresponding spin polarization curve is not reliable and a dashed line is used. Together with the 20-eV data in Fig.5(i), the results from different photon polarizations and energies rule out the possibility of the extrinsic spin polarization from photoemission process or spin matrix element effect, and confirm that the spin polarization comes from the electronic initial states.
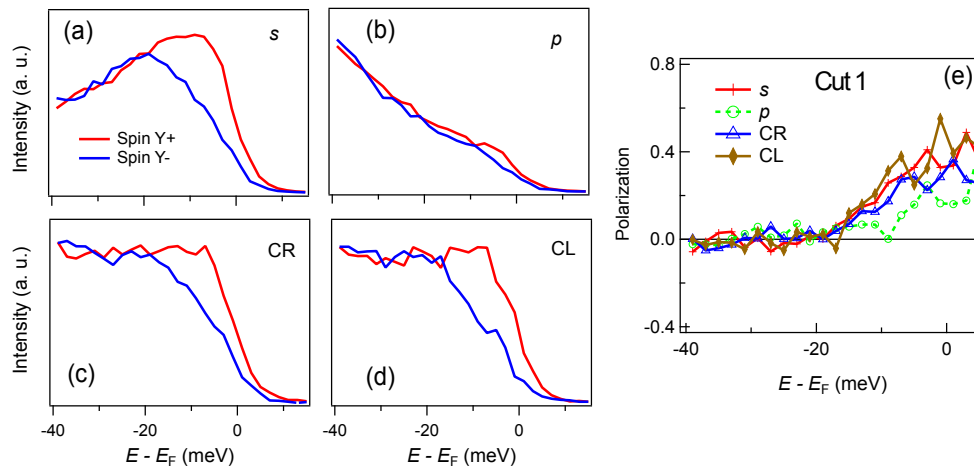
FIG. S8. **Photon polarization dependence of the spin polarization.** (a - d) Spin-resolved EDCs with different photon polarizations. (e) The corresponding spin polarization curves.

[1] Liang Fu and C. L. Kane, "Superconducting Proximity Effect and Majorana Fermions at the Surface of a Topological Insulator," Phys. Rev. Lett. **100**, 096407 (2008).

[2] Pavan Hosur, Pouyan Ghaemi, Roger S. K. Mong, and Ashvin Vishwanath, "Majorana Modes at the Ends of Superconductor Vortices in Doped Topological Insulators," Phys. Rev. Lett. **107**, 097001 (2011).

[3] Gang Xu, Biao Lian, Peizhe Tang, Xiao-Liang Qi, and Shou-Cheng Zhang, "Topological Superconductivity on the Surface of Fe-Based Superconductors," Phys. Rev. Lett. **117**, 047001 (2016).

[4] Y. Lubashevsky, E. Lahoud, K. Chashka, D. Podolsky, and A. Kanigel, "Shallow pockets and very strong coupling superconductivity in $FeSe_xTe_{1-x}$," Nat. Phys. **8**, 309–312 (2012).

[5] H. Miao, P. Richard, Y. Tanaka, K. Nakayama, T. Qian, K. Umezawa, T. Sato, Y.-M. Xu, Y. B. Shi, N. Xu, X.-P. Wang, P. Zhang, H.-B. Yang, Z.-J. Xu, J. S. Wen, G.-D. Gu, X. Dai, J.-P. Hu, T. Takahashi, and H. Ding, "Isotropic superconducting gaps with enhanced pairing on electron Fermi surfaces in $FeTe_{0.55}Se_{0.45}$," Phys. Rev. B **85**, 094506 (2012).

[6] Shahar Rinott, K. B. Chashka, Amit Ribak, Emile D. L. Rienks, Amina Taleb-Ibrahimi, Patrick Le Fevre, Fran ccois Bertran, Mohit Randeria, and Amit Kanigel, "Tuning across the BCS-BEC crossover in the multiband superconductor $Fe_{1+y}Se_xTe_{1-x}$: An angle-resolved photoemission study," Sci. Adv. **3**, e1602372 (2017).

[7] P. Zhang, P. Richard, T. Qian, Y.-M. Xu, X. Dai, and H. Ding, "A precise method for visualizing dispersive features in image plots," Rev. Sci. Instrum. **82**, 043712 (2011).

[8] Zhijun Wang, P. Zhang, Gang Xu, L. K. Zeng, H. Miao, Xiaoyan Xu, T. Qian, Hongming Weng, P. Richard, A. V. Fedorov, H. Ding, Xi Dai, and Zhong Fang, "Topological nature of the $FeSe_{0.5}Te_{0.5}$ superconductor," Phys. Rev. B **92**, 115119 (2015).

[9] Chris Jozwiak, Jonathan A. Sobota, Kenneth Gotlieb, Alexander F. Kemper, Costel R. Rotundu, Robert J. Birgeneau, Zahid Hussain, Dung-Hai Lee, Zhi-Xun Shen, and Alessandra Lanzara, "Spin-polarized surface resonances accompanying topological surface state formation," Nat. Commun. **7**, 13143 (2016).